Electronic structure of interstitial hydrogen in lutetium oxide from DFT+U calculations and comparison study with μSR spectroscopy

E. Lora da Silva*
Department of Chemistry, University of Bath, Bath BA2 7AY, United Kingdom

A. G. Marinopoulos, R. B. L. Vieira, R. C. Vilão, H. V. Alberto, and J. M. Gil
CFisUC, Department of Physics, University of Coimbra, P-3004-516 Coimbra, Portugal

R. L. Lichti, P. W. Mengyan, and B. B. Baker
Department of Physics, Texas Tech University, Lubbock, Texas 79409-1051, USA
(Received 12 May 2016; revised manuscript received 24 June 2016; published 7 July 2016)

The electronic structure of hydrogen impurity in Lu_2O_3 was studied by first-principles calculations and muonium spectroscopy. The computational scheme was based on two methods which are well suited to treat defect calculations in f-electron systems: first, a semilocal functional of conventional density-functional theory (DFT) and secondly a DFT+U approach which accounts for the on-site correlation of the $4f$ electrons via an effective Hubbard-type interaction. Three different types of stable configurations were found for hydrogen depending upon its charge state. In its negatively charged and neutral states, hydrogen favors interstitial configurations residing either at the unoccupied sites of the oxygen sublattice or at the empty cube centers surrounded by the lanthanide ions. In contrast, the positively charged state stabilized only as a bond configuration, where hydrogen binds to oxygen ions. Overall, the results between the two methods agree in the ordering of the formation energies of the different impurity configurations, though within DFT+U the charge-transition (electrical) levels are found at Fermi-level positions with higher energies. Both methods predict that hydrogen is an amphoteric defect in Lu_2O_3 if the lowest-energy configurations are used to obtain the charge-transition, thermodynamic levels. The calculations of hyperfine constants for the neutral interstitial configurations show a predominantly isotropic hyperfine interaction with two distinct values of 926 MHz and 1061 MHz for the Fermi-contact term originating from the two corresponding interstitial positions of hydrogen in the lattice. These high values are consistent with the muonium spectroscopy measurements which also reveal a strongly isotropic hyperfine signature for the neutral muonium fraction with a magnitude slightly larger (1130 MHz) from the *ab initio* results (after scaling with the magnetic moments of the respective nuclei).

DOI: 10.1103/PhysRevB.94.014104

I. INTRODUCTION

Lanthanide sesquioxides of the M_2O_3 stoichiometry (M a trivalent lanthanide cation) have attracted considerable interest in many industrial applications in catalysis, solid-state lighting, oxygen and hydrogen storage, and as permanent magnets [1]. These oxides are also promising in high-κ technology as potential gate materials in the next generation of field-effect transistors. They possess high dielectric constants ($\sim$30) [2] and can act as insulators with gap widths up to 6 eV [2], enabling band offsets with respect to the adjoining semiconductor of over 1 eV, thus minimizing carrier injection into its bands by acting as potential barriers [2,3]. Lanthanide sesquioxides are also thermodynamically stable in contact with Si, inhibiting the formation of thin insulating layers at the interface [2].

A good control of the oxide behavior in these diverse applications requires a fundamental understanding of the types of defects that can be created, either inside the oxide or at the interface with the surrounding vapor or other material components. Defects or dopants may appear in semiconductors and insulators at any stage of the system, from initial growth conditions to ageing of fully developed devices [2,4–6], affecting their properties and reliability. Hydrogen is an ubiquitous impurity, which can be unintentionally incorporated during the growth environment [7], in particular in the presence of water for Lu_2O_3 [8]. Hydrogen exhibits complex behavior when introduced in semiconductors and dielectrics [9,10]. It can act as an amphoteric impurity interacting with other dopants present in the material, where it may counteract the electric conductivity by passivating these dopant sources; or it can enable a donor level close to the conduction band, thus inducing n-type conductivity [7]. When samples are exposed to source gases containing hydrogen (up to about 1000 ºC for all practically obtainable water-vapor levels), either in the form of interstitial protons or hydroxide ions [11,12], it will dominate the ionic conductivity of the material at low temperatures [11,12].

Very limited theoretical studies of the defect physics of lanthanide oxides have been performed to date [6,13]. The main reason is that, from a theoretical perspective, their electronic structure is quite challenging. These materials are mixed valence systems, characterized by the highly localized $4f$-electron states of the lanthanide that couple with the existing valence states (*spd* states) [14,15]. The strong electron-electron correlation within these f-electron shells is poorly described by local (LDA) or semilocal (GGA)

*elds22@bath.ac.uk

functionals based on density-functional theory (DFT). Instead, these functionals, due to an incomplete cancellation of the Coulomb self-interaction, favor delocalization [15] for the (partially) occupied f states, therefore resulting in an incorrect description of the insulating properties of the oxides [14,16].

In principle, the self-interaction error and the inadequate description of correlations can be partly corrected by employing hybrid-functional approaches, where a portion of the Hartree-Fock exact exchange is included [14]. For magnetically ordered phases, such hybrid functionals significantly improve the description of the electronic structure of d- and f-electron systems, when compared to direct and inverse photoemission experiments [14]. This improvement is achieved by splitting the partially occupied d and f states into occupied and unoccupied manifolds [14]. Accurate electronic-structure studies of lanthanide/rare-earth sesquioxides and CeO_2 have also been carried out by employing hybrid functionals (HSE03 and HSE06), and the screened exchange LDA (sX-LDA) [16]. It has been observed that these methods describe the strongly correlated f electrons quite well, yielding the correct band gaps and trends across the lanthanide series. sX-LDA also tends to predict the unoccupied $4f$ levels at higher energies, leading to a better agreement with experiments [16], when compared to the G0W0@LDA+U results [17].

However, the use of hybrid functionals in studies of defects in solids have been limited to systems with sp-d bonding and band-gap character, since these are moderately still affordable [18–20]. In contrast, lanthanide systems where the $4f$ electrons are part of the valence-electron shells are extremely challenging. This is the reason why the previously mentioned studies were restricted to bulk systems where the respective primitive cells contain no more than 40 atoms [16]. Furthermore, recent work by Robertson and co-workers showed that the HSE06 functional and other hybrid functionals and GW-based methods improve somehow the energy gap for the lutetium oxide (increasing it in a range from 4.5 to 5.2 eV), although considerable discrepancy with experiment still exists (the experimental gap is close to 6 eV) [16].

For the present work, DFT calculations were carried out to study the hydrogen impurity in Lu_2O_3. More specifically, we have used two different approaches. The first was to employ a semilocal (GGA) DFT functional with the localized $4f$ shell treated as a corelike shell. This method is usually referred to as the standard model or ionic model [21] and has been employed in the past for the study of lanthanide, rare-earth oxides [22] and oxide surfaces [23]. This approach has also been used to treat the correlated states of trivalent lanthanide impurities in CeO_2, to predict the connection between defect association and ionic conductivity [24]. The main justification for this approach is that it avoids an important drawback of local (LDA) and semilocal (GGA) DFT functionals. By employing these functionals, without imposing the frozen-core approximation, the localization of the $4f$ states is predicted to be too weak, therefore, yielding a very strong hybridization with the other valence states and much too large density of states at the Fermi level. It is noteworthy to mention that the standard model does not account for all aspects of lanthanide-rare-earth electronic properties (such as magnetism) which need a more refined coupling of the f states with the remaining valence states [21]. The second approach was based on a DFT+U methodology that accounts for the on-site $4f$-electron correlations via an effective Hubbard-type potential. The $4f$-electron shell was treated as being part of the valence shells and the magnitude of the effective Hubbard parameter was chosen to minimize the overlap between the $4f$ and sp-valence states.

The DFT+U approach is computationally as efficient as conventional DFT, well suited for defect studies which require a large number of atoms and has also proved reliable in recent studies of defects in f-electron solids [25–29]. Our choice is also guided by our goal to examine the full configurational space of hydrogen in lutetium oxide and identify all local-energy minimum configurations which can be probed by the μSR technique. This is well suited by DFT+U which can treat structural relaxations adequately and at the same time retain the correct physics of on-site correlation for the $4f$ electrons of the lanthanide ions.

Using these approaches we determined the configurations and electronic structure of isolated hydrogen states in Lu_2O_3. The geometrical configurations of interstitial hydrogen were explored in detail for all possible charge states that hydrogen can assume. From the minimum-energy configurations, we further determined the electrical levels of hydrogen, the induced defect levels in the gap, and resulting hyperfine constants.

Isolated hydrogen impurities are difficult to probe experimentally due to their high mobilities which favor pairing with other defects [13,30,31]. The use of microscopic techniques like electron paramagnetic resonance (EPR) or infrared (IR) vibrational spectroscopy in order to obtain microscopic information about hydrogen configurations and levels such as those calculated in this work is thus limited to a couple of systems where hydrogen is usually present in high concentrations [32–35]. However, this microscopic information about hydrogen configurations can be obtained by using muonium (the bound state of a positive muon with an electron) as a light pseudoisotope of hydrogen [36,37]. Beams of positive muons are available in international muon spin research (μSR) installations and muonium spectroscopy has been successfully used in order to determine muonium (and therefore hydrogen) charge-transition levels and sites, often in a synergistic approach with *ab initio* studies [18,19,38–41]. Moreover, muonium spectroscopy can provide detailed information about the electronic structure of muonium/hydrogen through the hyperfine interaction [42–46]. Such information is almost nonexistent for isolated hydrogen from any other technique [47].

Muon spin rotation measurements were completed on a polycrystalline sample of Lu_2O_3. During this experiment, magnetic fields up to 7 T were applied across the sample in a direction perpendicular (transverse) to the incoming muon spin polarization direction, at room temperature (300 K) and at 2.5 K. Data analyses were performed with the MSRFIT and WiMDA codes [48].

The paper is thus organized as follows. Section II contains an explanation of the theoretical methodology adopted in the present work together with a description of the lattice of Lu_2O_3. The obtained results on hydrogen structural configurations, formation energies, local electronic states, and hyperfine constants are presented in Sec. III. In the same section the

μSR data and related analysis are also provided. Finally, our conclusions are presented in Sec. IV.

II. THEORETICAL METHOD

The primitive unit cell of Lu_2O_3 consists of a 40-atom body-centered cubic (BCC) structure [49], corresponding to the space-group Ia3-(Th7) (No. 206), with a conventional cell that can be represented as an 80-atom cubic *c*-type structure (Fig. 1) [49,50]. The structure is formed by 64 slightly distorted minicubes composed of O anions at the vertices. Only 32 centers of these minicubes are occupied by the Lu metal (M) cations, and the remaining are empty (denoted as structural void-M sites). The cations are positioned at two different crystallographic symmetry sites, with M_1 belonging to the 8*b* site and M_2 at the 24*d* site (Fig. 1). The anions are positioned at the 48*e* crystallographic sites. The eight vertices of the minicubes are occupied by six anions only, therefore enabling an octahedral coordination for the cations [15,49]. The unoccupied O vertices will be henceforth denoted as unocc-O sites. For the M_2-centered minicubes, three O ions are positioned at one face of the cube, and the other three are at the opposite face, all of the six anions being equally distanced from the cation center (2.24 Å). The vertices of the M_1-centered minicubes are formed by four O ions at one face and the other two at the opposite face—the distance between the anions and the respective cation center occurs with three different paired distances (2.30, 2.22, and 2.20 Å) [51]. Figure 1 represents part of the conventional cell of luthetia denoted with the above mentioned crystallographic sites (created by using the visualization program VESTA [52]).

In the present theoretical study, two spin-polarized DFT approaches were employed: the generalized-gradient approximation (GGA) with the Perdew, Burke, and Ernzerhof (PBE) parametrization [53] and the DFT+U method, with PBE applied as the exchange-correlation functional, and a Hubbard on-site potential proposed by Dudarev *et al.* [54].

Within the DFT+U method, the potential energy is supplemented with a Hubbard-like term. For the present calculations, we employed the rotationally invariant approach proposed by Dudarev *et al.* [54], where the correction for the on-site interactions between the Lu f electrons is expressed by a single U_{eff} parameter, where $U_{\text{eff}} = U - J$, with U and J being screened Coulomb and exchange parameters, respectively. This energy term has the form

$$\mathrm{E_{DFT+U}} = \mathrm{E_{DFT}} + \frac{U-J}{2}\sum_{\sigma}[\mathrm{Tr}(\rho^{\sigma}(1-\rho^{\sigma}))],$$

where ρ is the 7×7 density matrix of the f states and σ denotes one of two spin orientations [15]. When setting $U_{\text{eff}} = 0$ eV, one recovers the semilocal functional limit. U_{eff} is usually determined empirically, to fit some specific physical property, typically the band-gap width [55].

The value for U_{eff} was chosen to be 5.4 eV, which is an adequate value in order to treat the localized f states of the lanthanide systems (Refs. [14] and [17] for more details), whereas the p and d states, constituting the upper valence band and conduction band, respectively, were treated at the PBE level.

The referenced methods are implemented in the Vienna *Ab-Initio* Simulation Package (VASP) [56–58] code, which performs electronic structure calculations by employing plane-wave basis sets to expand the Kohn-Sham wave functions, thus taking advantage of the periodicity of extended systems. Projector augmented wave (PAW) pseudopotentials [59,60] were applied and the lower semicore s and p shells of Lu were treated as valence electrons. Moreover, due to the nature of the two DFT approaches, two different sets of pseudopotentials for Lu were used: for the semilocal PBE calculations, the f electrons are kept frozen inside the core region; whereas, for DFT+U, the f states are reconstructed as part of the valence wave function.

For both methods, a plane-wave cutoff energy of 450 eV and an automatic mesh of $4\times4\times4$ Monkhorst-Pack grids [61] were applied. The total energies and the structural lattice relaxations were calculated by using these converged basis sets. The lattice parameters (Sec. III) were obtained by fitting the Birch-Murningham equation of state to energy vs. volume results [62].

The formation energies of the hydrogen impurity were evaluated in supercells of 80-atom structures of the host material. The formation energy of interstitial hydrogen is defined as the energy needed to incorporate the impurity in the host lattice and was determined for hydrogen in all the charge states $q = \{-1, 0, +1\}$ by following the procedure from Refs. [7,41,63,64]. The corresponding expression is

$$\mathrm{E_{form}}(\mathrm{H}^q) = \mathrm{E_{tot}}(\mathrm{H}^q) - \mathrm{E_{tot}}(\mathrm{bulk}) - \tfrac{1}{2}\mathrm{E_{tot}}(\mathrm{H_2}) + q(\mathrm{E_F} + E_{\mathrm{VBM}} + \Delta V).$$

$\mathrm{E_{tot}}(\mathrm{H}^q)$ is the total energy of the supercell with the hydrogen impurity of charge q, $\mathrm{E_{tot}}(\mathrm{bulk})$ is the total energy of the bulk supercell, and $\frac{1}{2}\mathrm{E_{tot}}(\mathrm{H_2})$ is the reference energy for hydrogen that is given by an H_2 molecule at $T = 0$ [41,65]. The Fermi level, $\mathrm{E_F}$, is referenced to the valence-band maximum of the bulk supercell, E_{VBM}. ΔV denotes a correction term that aligns the average electrostatic potential of the defect supercell with that in the bulk [64] (and corresponds to the change of the reference potential after introducing a defect).

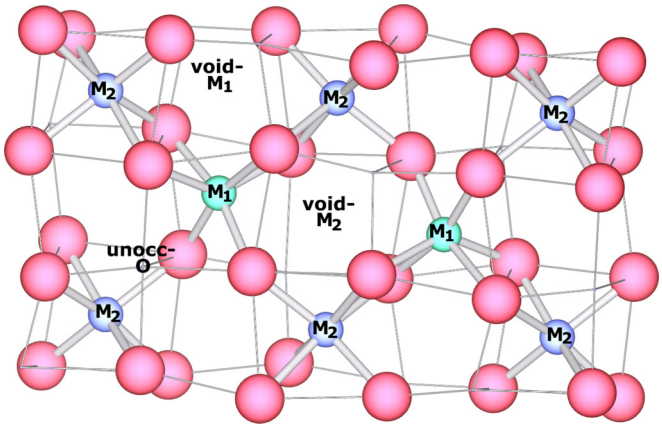

FIG. 1. Part of the conventional cell of Lu_2O_3. O is represented by the larger red spheres and Lu by the smaller blue and green spheres, to distinguish between the two different metal sites, M_1 and M_2, respectively. The structural interstitial sites: voids and unoccupied sites of the lattice are labeled accordingly.

The use of supercells is a natural choice in solid state calculations; nevertheless one needs to take into account problems arising from charged defects incorporated in the system [66]. A neutralizing background charge needs to be introduced in order to cancel electrostatic divergences [66]. Image-type corrections based on multipole expansion were therefore added (up to the monopole-quadrupole interaction) to the total energies of the charged systems. These corrections were found to be in the range 0.1 eV to 0.2 eV.

The hyperfine coupling represents an interaction between the electron spin density $\sigma(\mathbf{r})$ with spin S, and nuclei J with nuclear spin I:

$$H = \sum_{i,j=1}^{3} S_i A_{ij} I_j,$$

where i and j are the tensor components.

The hyperfine tensor, A_{ij}, can be written as the sum of two interactions, a contact interaction (isotropic) and a classical interaction (anisotropic) [67]:

$$A_{ij} = \frac{1}{2S}\gamma_J \gamma_e \hbar^2 [(A_{\text{iso}})_{ij} + (A_{\text{ani}})_{ij}].$$

γ_J is the nuclear Bohr magneton of nucleus J and γ_e the electron Bohr magneton.

The contact term, known as the Fermi contact, is defined as

$$(A_{\text{iso}})_{ij} = \frac{8\pi}{3}\delta_{ij} \int \delta(\mathbf{r}-\mathbf{R})\sigma(\mathbf{r})d\mathbf{r},$$

which is proportional to the magnitude of the electron spin density at the position of the nucleus. δ_{ij} represents the usual Kronecker δ (unit matrix).

The classical dipole-dipole contribution is

$$(A_{\text{ani}})_{ij} = \int \left[\frac{3(\mathbf{r}-\mathbf{R})_i(\mathbf{r}-\mathbf{R})_j}{|\mathbf{r}-\mathbf{R}|^5} - \frac{\delta_{ij}}{|\mathbf{r}-\mathbf{R}|^3}\right]\sigma(\mathbf{r})d\mathbf{r}.$$

More complete overview regarding the numerical implementation can be found in Refs. [67–69].

Convergence for the hyperfine parameters were obtained for a higher plane-wave cutoff of 550 eV with the same **k**-point sampling of 4×4×4 Monkhorst-Pack grids. The nuclear gyromagnetic ratios were taken from experimental values found at Ref. [70], with ^{1}H = 42.577 MHz/T, ^{175}Lu = 4.862 MHz/T, and ^{16}O = 0.000 MHz/T.

III. RESULTS AND DISCUSSION

A. Electronic bulk properties

The bulk properties were calculated by applying the two methods mentioned above. With PBE, we obtained $a_0 = 10.37$ Å as the lattice parameter value, whereas with DFT+U this value decreases to $a_0 = 10.23$ Å. The PBE result is comparable to experimental data found in Ref. [49], with $a_0 = 10.39$ Å and to other theoretical results when employing a similar methodology (10.37 Å [15] and 10.36 Å [22]). The DFT+U value is slightly lower, but compatible to other results obtained with the Hubbard-U approach ($a_0 = 10.26$ Å found in Ref. [15]). It was argued that inclusion of the U term often tends to decrease the value of the lattice parameters [15].

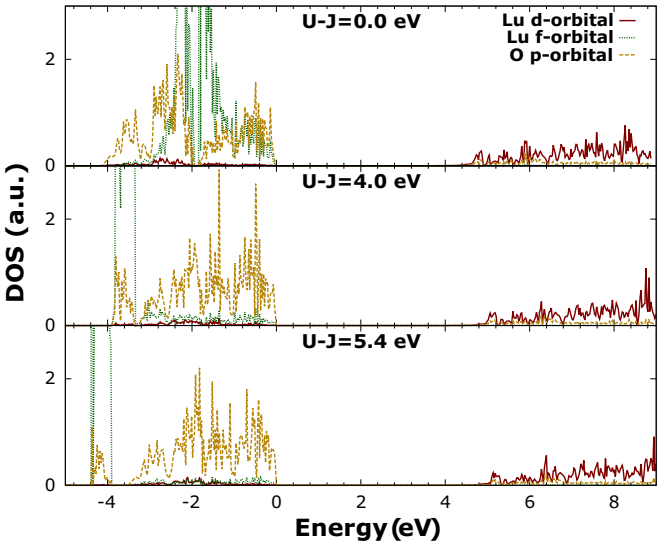

FIG. 2. DFT+U partial site and angular momentum projected density of states of bulk Lu_2O_3. The three plots show the convergence of U_{eff} with respect to the overlap of f-Lu with p-O states, performed by defining $U_{\text{eff}} = 0.0$ eV, $U_{\text{eff}} = 4.0$ eV, and $U_{\text{eff}} = 5.4$ eV. The valence-band maximum is aligned at the zero-energy level.

The calculated band-gap width, $E_g = 4.0$ eV, is smaller than the value measured experimentally and found in the range 5.8–6.0 eV [71,72]. This is expected when employing the semilocal functional. Also, the inclusion of the Hubbard-U potential (which only acts on the f electrons) does not increase the magnitude of the gap since the latter is principally defined by the position of the valence p and conduction d states. The band gap obtained by DFT+U is therefore again equal to 4.0 eV. It is noteworthy to mention that an earlier study, by employing the DFT+U with a LDA functional, resulted in a smaller gap width (3.2 eV) [14].

The site and angular-momentum projected density of states (PDOS) (Fig. 2) provides a clear understanding of the effect of the Hubbard term upon the f states. The upper valence band of the oxide is formed by the O p states, which are hybridized with the f states of the metal. The conduction band is formed mainly by metal d states with a small contribution of O p states. By setting $U_{\text{eff}} = 0$ eV, which is the limit of a purely PBE calculation, one observes that the f states are completely delocalized within the p valence band. By increasing the Hubbard-U term, the f states begin to localize and shift in energy towards more negative values. The value $U_{\text{eff}} = 5.4$ eV was found to be sufficient to localize the f states below the p valence-band states, therefore not affecting the occupied states that constitute the upper valence band. The width of the valence band is also observed to decrease when the f states do not interact strongly with the p states.

B. Hydrogen configurations and formation energy

Different initial interstitial hydrogen configurations were considered, by placing the H impurity at several positions in the lattice, near symmetry sites and different inequivalent void and unoccupied sites (Fig. 1). This was done for all charged

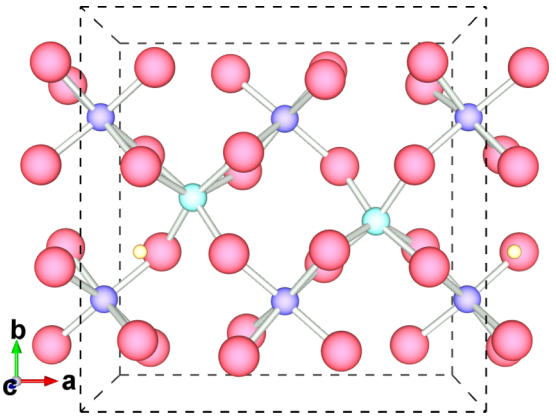

FIG. 3. DFT+U stable H configuration for the H^0 and H^- states. The H impurity (represented by the small yellow sphere) stabilizes at an unoccupied O site.

states of hydrogen (H^+, H^-, and H^0). Full structural relaxations were then carried out by both DFT and DFT+U.

Three stable configurations were found for H^0, in close analogy with those found in the isostructural yttrium oxide [18]. One stable configuration exists for the interstitial unoccupied O site (unocc-O) and another for the interstitial void metal at the M_1 center (void-M_1) (Figs. 3 and 4, respectively). The resulting relative energies between these two configurations imply that unocc-O is lower in energy than void-M_1, by either DFT or DFT+U.

A third stable H^0 configuration found is a bond O-H system (bond-O), where H binds to an O ion (Fig. 5). The energy of this bond configuration is higher when compared to the interstitial neutral configurations, a result predicted by both DFT and DFT+U methods.

The same configurations, with similar relative energy ordering, were found for the negatively charged systems. In contrast, for the H^+ state, only the bond-O configurations are found as energy minima. It is noteworthy that several nonequivalent bond-O configurations were obtained for either charge state; therefore, only the lowest-energy systems are discussed throughout the paper, and are taken as the representative systems for the respective charge states. Figures 3, 4, and 5 were created by using the visualization program VESTA [52].

For the bond-O neutral system, the impurity atom prefers to bind to an anion belonging to the equally distributed sixfold minicube environment (void-M_2). On the other hand, for the charged states, H prefers to bond to an O belonging to a void-M_1 center (bonded to the anion that sits at the two-coordination face) (Fig. 5). The preferred configuration of the charged impurity will allow the lowering of steric effects which will in turn lower the overall energy cost due to the overlapping electron densities. The two O neighbor ions are brought closer together due to H interaction, by about 0.30 Å. The O-H bond of the negatively charged system is 1.00 Å and the bond increases slightly for the positive charged system, up to 1.01 Å. For the neutral system, the length of the O-H bond is the same as the negatively charged system, about 1.00 Å of length. These configurations show a stronger lattice distortion, when compared to the interstitial H configurations,

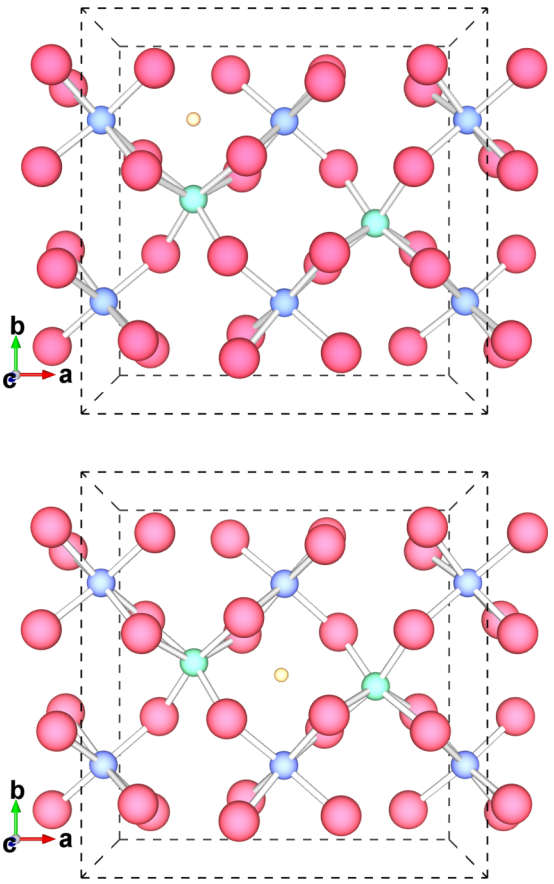

FIG. 4. Stable H configuration for the H^0 and H^- states. The H impurity stabilizes at a void metal center. The top plot represents the void-M_1 configuration (DFT+U) and the bottom plot the void-M_2 configuration (PBE). The latter configuration is only found at the PBE level for the neutral state and is not stable with DFT+U.

which is more pronounced for the positively charged states. At the close vicinity of the impurity center, several Lu-O bonds "deform" from their original lengths in order to accommodate the perturbation caused by the impurity.

The stable configurations found by PBE and the DFT+U are structurally very similar. The only exception was that within PBE an additional impurity configuration was found for the neutral state: a void-M_2 state, which is represented in Fig. 4 (bottom). When employing DFT+U, this configuration is unstable with H displacing to the closest O unoccupied vertex. The reason for this effect may be due to the existing coupling between the low-lying cation f states to the O-p, which will increase the VBM to higher Fermi energies [73], thus allowing for the enhancement of the chemical repulsions between the valence states with the impurity spin density (Fig. 2). The valence interactions with the impurity, described within PBE (without f electrons), would effectively be weaker, therefore enabling the stability of the void-M_2 configuration.

The overall results for the formation energies are very similar, when comparison is made between the two methods: amphoteric behavior of H is found for the global ground-state energy structures. This compensating behavior can be understood based on the position of the charge-transition levels, $E(q/q')$, within the gap. Based on Fig. 6, we observe

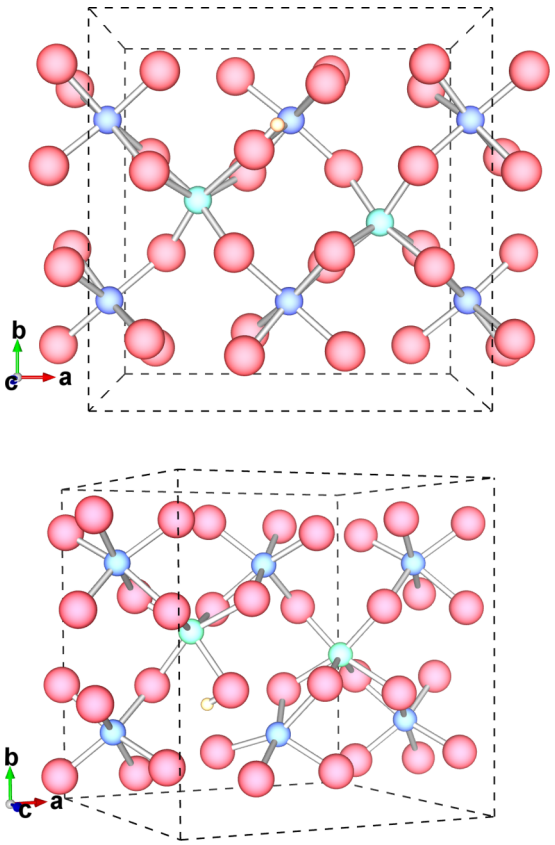

FIG. 5. DFT+U bond-O configurations of the H impurity for the H^0 (top) and H^- (bottom) charge states. The stable configuration for the H^+ system is similar to the H^- state. The presented structures are the representative lowest-energy bond-O configurations.

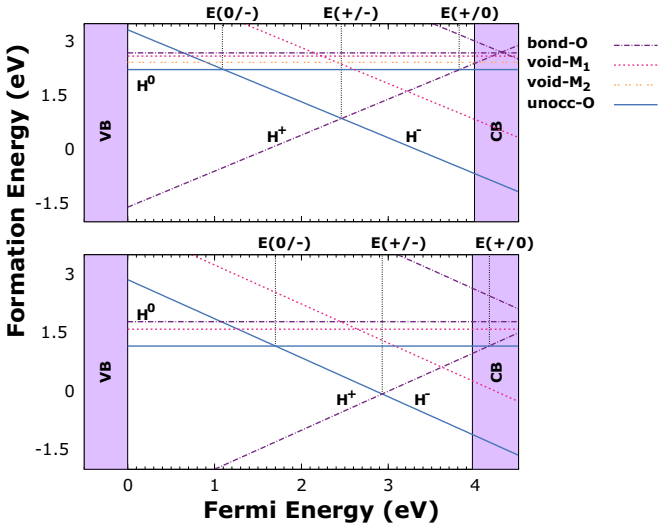

FIG. 6. Formation energy of the different hydrogen configurations as a function of the Fermi-level position. The range of E_F corresponds to the bulk theoretical band gap with $E_F = 0$ aligned at the valence-band maximum. The formation energies of the different geometrical configurations are represented by different line types and colors. The upper plot represents the results obtained by employing the PBE exchange-correlation functional, where the f electrons were treated as corelike states. The lower plot represents the results obtained from DFT+U with the f electrons treated as valence states. The thermodynamic charge-transition (electrical) levels are marked by the vertical lines.

that the pinning level, $E(+/-)$, is positioned in the middle of the band gap. Also, a *negative-U* behavior is observed since there is an inversion of the ordering of the levels: the donor level, $E(+/0)$, lies above the acceptor level, $E(0/-)$ [7,63]. This suggests that the neutral configurations are never thermodynamically stable at any range of the Fermi energy.

The energy ordering for the different impurity configurations is similar between the PBE and the DFT+U results, but it is clearly evidenced that the transition levels for DFT+U are positioned at Fermi-level positions of higher energies (in the gap) (Fig. 6, bottom).

For both methods, the formation energies show that the most stable hydrogen configuration of the neutral and negative charged systems is at the unocc-O site. For the positive charged states, only the bond-O configuration exists, although it occurs with different surrounding environments. For the neutral and negatively charged systems, higher-energy configurations also occur, and the bond-O configurations are energetically less favorable for both charged systems than the configuration with hydrogen at the void-M_1 site (see Fig. 6). The fact that this bond-O configuration is higher in energy than the interstitial configurations is consistent with findings for other oxides, i.e., yttria [18] and uranium oxide [25]. For PBE, the extra neutral configuration observed at the void-M_2 site is lower in energy (by about 0.17 eV) than that at the void-M_1 center. This configuration is not stable using DFT+U, allowing one to conclude that the valence contribution of the f states has an influence in defining the configuration space of the impurity.

For PBE, the pinning level $E(+/-)$ lies deep in the gap, $E(+/-) = E_{VBM} + 2.5$ eV, when aligned to the valence-band maximum (VBM). The donor level is positioned at $E(+/0) = E_{CBM} - 0.2$ eV, which is very close to the conduction-band minimum (CBM), with the acceptor level located at $E(0/-) = E_{VBM} + 1.1$ eV (Fig. 6). When employing DFT+U, the transition levels are shifted to higher energies, with $E(+/-) = E_{VBM} + 2.9$ eV. The donor level, $E(0/+)$, of the lowest energy configuration, is thereby shifted to an energy level above the CBM, $E(+/0) = E_{CBM} + 0.2$ eV, indicating that the electron in very loosely bound. Nonetheless, the pinning level is not sufficiently above (or close enough to) the CBM to allow for hydrogen to be a source of doping [7].

For the higher energy, bond-O, configurations, the respective pinning and the donor levels lie above the CBM (observed for both methods). From these results we can infer that a portion of these bond-type configurations are shallow donorlike configurations with corresponding donor and pinning levels interacting with the CB states.

C. Local density of states and electron-density isosurfaces

In order to probe the character of the defect-induced levels inside the gap, the site and angular-momentum projected (PDOS) of the different neutral geometrical configurations were evaluated, by employing both levels of theory (Figs. 7, 8, and 9). Since spin-polarized calculations were

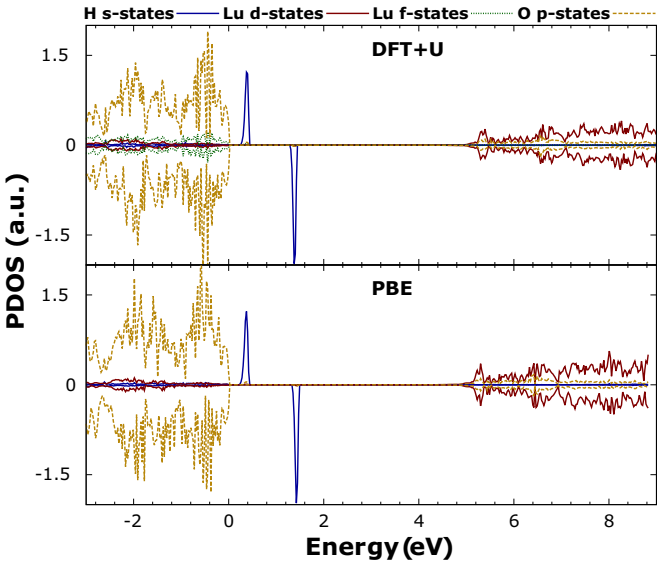

FIG. 7. Spin-polarized partial site and angular momentum projected density of states of the unocc-O configuration calculated by employing DFT+U (top) and PBE (bottom). The valence-band maximum is aligned at the zero-energy level.

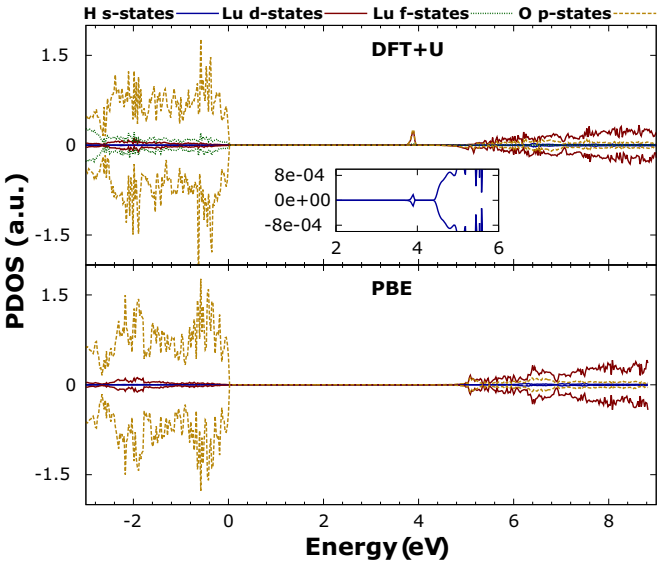

FIG. 9. Partial site and angular momentum projected density of states of the lowest energy bond-O configuration calculated by employing DFT+U (top) and PBE (bottom). The valence-band maximum is aligned at the zero-energy level.

carried out the PDOS plots display both spin-channel components.

For the unocc-O and void-M_1 configurations, the defect levels are positioned quite close to the valence-band (depicted in Figs. 7 and 8). For the unocc-O configuration, and by applying DFT+U, the impurity level is located 0.3 eV above the VBM, and for PBE it is 0.2 eV (considering the spin-up states, where the impurity level is closest to the VBM). For the void-M_1 configuration, the level is positioned at higher energies, although still close to the VBM: 1.4 eV and 1.3 eV for DFT+U and PBE, respectively.

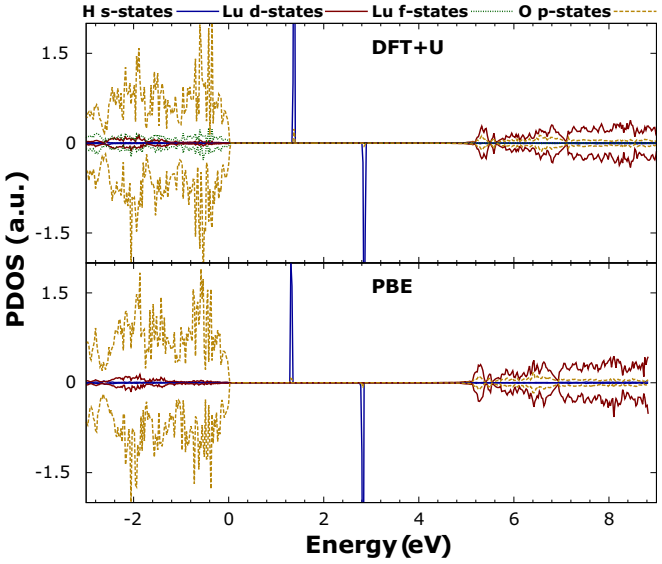

FIG. 8. Spin-polarized partial site and angular momentum projected density of states of the stable void-M_1 configuration calculated by employing DFT+U (top) and PBE (bottom). The valence-band maximum is aligned at the zero-energy level.

Conversely, the oxygen-bond configurations differ from the unoccupied and void configurations. By looking at the PBE results, it is not possible to observe a defect level inside the gap (Fig. 9). However, for DFT+U, a small level (mainly of p and d contribution, and very low portion due to s states) is positioned inside the gap, and very close to the CBM (∼0.2 eV below the CBM, with the DFT+U bulk band gap being of the order of ∼4.0 eV). One may observe that a very low concentration of s states of the impurity is delocalized at the conduction band. This feature may suggest that the impurity electron is loosely bound to H, allowing for the impurity to act as a shallow donor. Once again, differences in assigning metal f states to the valence contributions are observed, where the chemical interactions seem to have some effect to the spin state of the impurity. With DFT+U the defect level is localized and positioned at close proximity to the conduction edge, whereas for PBE, the defect level is resonant with the conduction states, positioned above the CBM. The DFT-U description is consistent with the formation of self-trapped charge carriers, since we also observe significant lattice relaxations of the bond-O configurations [73].

The electron-density isosurfaces of the neutral systems were evaluated with DFT+U, in order to provide a more detailed information regarding the nature and localization of the impurity electron.

For the unocc-O and the void-M_1 configurations, where a defect level is positioned close to the VBM (Fig. 10), one may observe that the isosurfaces possess a strong s-type character with the electron centered at the impurity. Contributions of p states around the impurity, on the next-neighbor O anions (depicted in Fig. 10), are also seen and justified from the close proximity of the defect level to the valence-band edge, which has essentially p character (Fig. 7).

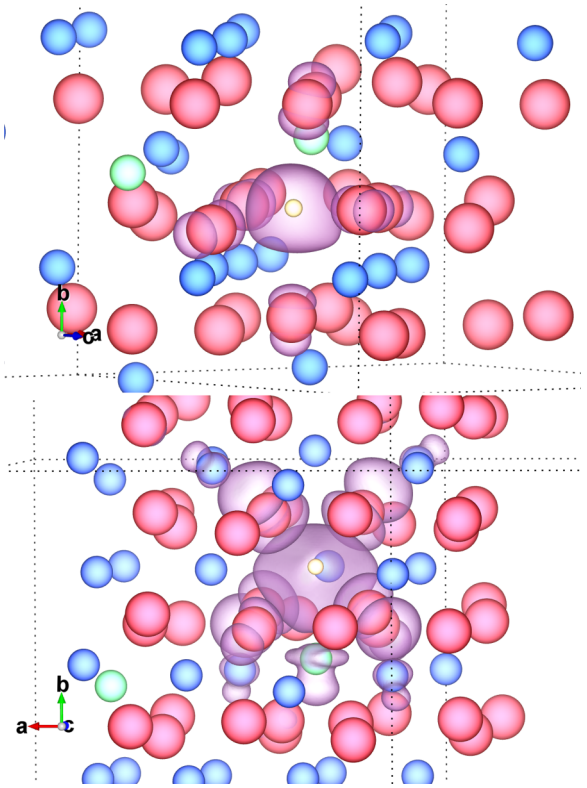

FIG. 10. DFT + U isosurfaces of the electron charge densities for the neutral state of unocc-O and void-M_1 configurations. The atoms are represented by their ionic radius, where O is depicted in red, Lu in blue/green, and hydrogen in yellow.

For the bond-O systems, and similar to what was found in Ref. [18] for yttria and in Ref. [19] for cubic zirconia, one may observe that the hydrogen electron is trapped at the closest cation neighbors (Fig. 11). In response to the formation of the impurity-anion bond, significant lattice distortion takes place for these configurations. These are related to a change of oxidation state of the corresponding anion (O^{2-} to OH^{-} state) causing the lengths of the neighboring bonds to adjust, thus resulting in large rearrangements of the host lattice [74]. The resulting displacement field near the hydrogen impurity causes the defect electron to become trapped close to the impurity atom, at a cation center [75]. This behavior resembles the effects suggested by Cox *et al.* [75] of a polaron-type formation, where the polaron center may be shallow and therefore act as a donor center as well. The impurity electron is trapped close to the hydrogen nucleus, at nearby metal centers, and has predominantly a conduction-band d-type character—the defect level is positioned quite close to the conduction band allowing the respective states to interact with each other (Fig. 11).

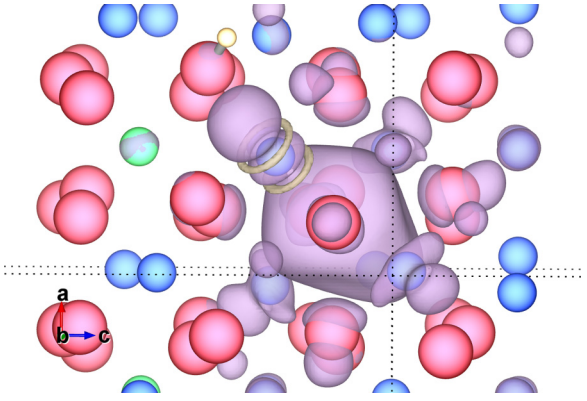

FIG. 11. DFT + U isosurfaces of the electron charge densities for the neutral state of the representative, lowest energy, bond-O configuration. The atoms are represented by their ionic radius, where O is depicted in red, Lu in blue/green, and hydrogen in yellow. The purple color of the isosurface refers to positive values and the yellow to negative values.

D. Hyperfine constants

The calculations of the hyperfine tensors proved useful in characterizing the neutral impurity centers, thus allowing a direct comparison with the experimentally obtained hyperfine constants measured by μSR. Only the DFT+U method was employed in this case, since it is within this level of theory that the f orbitals are treated correctly as valence states. Moreover, it is also well known that a pure PBE approach tends to delocalize the spin density of defect centers [67].

The calculations for the neutral interstitial hydrogen configurations (hydrogen at the unoccupied unocc-O and void-M_1 sites) revealed a predominant isotropic component with very small dipolar part. The Fermi-contact isotropic constant, A_{iso}, was found equal to 926 MHz and 1061 MHz for the unocc-O and void-M_1 configurations, respectively. These results indicate that it is the latter configuration which yields a higher spin localization. (See Table I.)

E. μSR results and analysis

The oxide sample used in the present study was obtained commercially from Alfa-Aesar (REActon 99.995%). The measurements were performed with the HiTime spectrometer on the M15 surface muon channel at TRIUMF (Vancouver, Canada).

The μSR spectrum at $T = 300$ K, for an external applied magnetic field $B = 7$ T, is shown in Fig. 12. A clear oscillating pattern is observed, which corresponds to the beating between two frequencies identified at $\nu_d = 948.96(2)$ MHz and at $\nu_{12} = 833.2(2)$ MHz. The corresponding fast-Fourier transform (FFT) is shown in Fig. 13. ν_d corresponds to the expected

TABLE I. Formation energies and hyperfine constants are presented for the different hydrogen configurations (neutral state). Energy values are referenced with respect to the ground-state configurations (unocc-O) and are presented in units of eV. The hyperfine constants are referenced in units of MHz.

	DFT	DFT+U	
	ΔE	ΔE	A_{iso}
Unocc-O	0.00	0.00	926
Void-M_1	0.37	0.43	1061
Void-M_2	0.20		
Bond-O	0.46	0.62	∼0

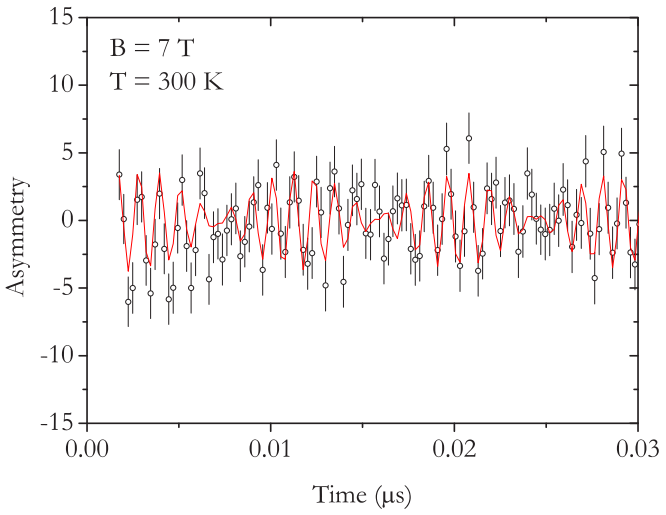

FIG. 12. μSR time spectrum of a polycrystalline sample of Lu_2O_3, for an applied transverse magnetic field $B = 7$ T, at $T = 300$ K. The beating of the diamagnetic frequency and of the muonium ν_{12} line is clearly seen. The red line is a fit as described in the text.

Larmor frequency of the diamagnetic muon at the applied field. ν_{12} is a frequency characteristic of the $1 \rightarrow 2$ transition in the field-dependent hyperfine spectrum of muonium, the paramagnetic bound state of a positive muon with an electron. In the high-field limit, this frequency corresponds to the "flip" of the muon spin with electron spin up and amounts to half of the spectral weight [45]. The other half of the spectral weight corresponds to the unobservable ν_{34} frequency characteristic of the $3 \rightarrow 4$ transition where the muon spin flips with electron spin down.

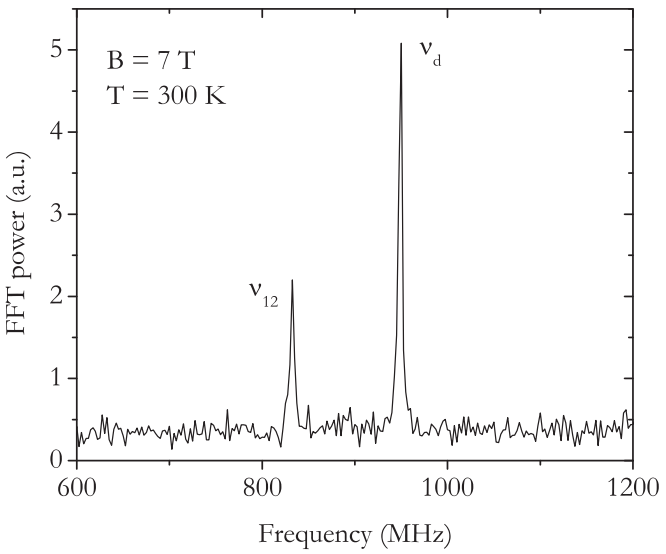

FIG. 13. Fast-Fourier transform (FFT) of the μSR time spectrum at room temperature, for an applied transverse magnetic field $B = 7$ T, showing the presence of the diamagnetic frequency at $\nu_d = 948.98(1)$ MHz and of the muonium ν_{12} frequency at $\nu_{12} = 833.2(2)$ MHz.

The time spectrum in Fig. 12 was thus analyzed using a sum of damped oscillations of the form:

$$A(t) = A_{\rm dia} e^{-\lambda_{\rm dia} t} \cos(2\pi \nu_{\rm dia} t + \phi_{\rm dia}) + A_{\rm Mu} e^{-\lambda_{\rm Mu} t} \cos(2\pi \nu_{\rm Mu} t + \phi_{\rm Mu}).$$

A room temperature calibration with a silver sample at $B = 7$ T allowed us to extract the maximum instrumental asymmetry $A_{\rm max}$ and therefore to measure the fraction of muons thermalizing at the diamagnetic configuration ($f_{\rm dia} = A_{\rm dia}/A_{\rm max}$) and the fraction of muons thermalizing at the paramagnetic muonium configuration ($f_{\rm Mu} = 2A_{\rm Mu}/A_{\rm max}$, where the multiplication by two accounts for the unobservable υ_{34} transition). We find that $f_{\rm dia} = 23(1)\%$ and $f_{\rm Mu} = 46(3)\%$. The corresponding relaxations were found to be $\lambda_{\rm dia} = 0.1(1)\ \mu{\rm s}^{-1}$ and $\lambda_{\rm Mu} = 6(1)\ \mu{\rm s}^{-1}$.

We begin the discussion of the experimental data by noting that the experimental observations are consistent with the presence of an isotropic hyperfine interaction. From the fitted value of ν_{12} we can easily estimate the value of the hyperfine interaction [45,76] to be $A_{\rm iso} = 3596.7(4)$ MHz. We have confirmed that ν_{12} varies as expected for this hyperfine interaction by performing room-temperature measurements at $B = 2$ T and at $B = 4$ T, obtaining $\nu_{12} = 1470.4(5)$ MHz and $\nu_{12} = 1227.7(5)$ MHz, respectively. Both are consistent with $A_{\rm iso} = 3597(1)$ MHz.

In order to compare this value with the calculated values for hydrogen, we must take into account that the hyperfine interaction for muonium is expected to be higher than that for hydrogen by the factor 3.184 corresponding to the ratio of the magnetic moment of the muon and that of the proton [47]. The expected value for the experimentally measured hyperfine interaction, taking the correction into account, is equal to $A_{\rm iso} = 1129.7(3)$ MHz. This means that the calculated values for the unocc-O and void-M_1 interstitial configurations (see previous subsection) are lower than the experimental value by 18% and 6%, respectively. These discrepancies are judged satisfactory given the approximate treatment of exchange and on-site correlation adopted in the present work.

In fact, similar discrepancies have also been reported recently between the hyperfine interactions calculated by *ab initio* methods and those measured experimentally [67]. These authors report differences of about 15% to 20% in the calculation of hyperfine interactions in solids using the PBE functional, which notably decrease when using a hybrid-functional (HSE06) approach. Also (and more in relevance to the present work), in a recent study [77] of hyperfine parameters of neutral hydrogen configurations in zirconia, the isotropic constants calculated within PBE were smaller than those obtained by HSE06 by as much as 10% (for a fixed plane-wave cutoff energy). Taking into account that the calculated values of the hyperfine interactions for the unocc-O and void-M_1 interstitial configurations are themselves different by less than 15%, it is not possible to assign the experimentally observed muonium state to a specific configuration from the value of the hyperfine interaction alone. The observed value is nevertheless consistent with the calculated values. It is also important to note that a slight variation of the value of the hyperfine interaction of muonium with respect to that of

hydrogen is expected due to the different zero-point motion of the muon and of the proton.

A measurement at 2.5 K indicates that the same isotropic state is present at low temperatures, albeit with a smaller fraction (∼20%) and a slightly larger hyperfine interaction $A_{\rm iso} = 3629(2)$ MHz, corresponding to $A_{\rm iso} = 1139.8(6)$ MHz after taking the referred magnetic moment ratio into account. The investigation of the corresponding temperature dependence is ongoing and will be published elsewhere. We however note that the slight decrease of the hyperfine interaction with increasing temperature is a well known effect of the onset of lattice vibrations [45,76]. The different formation probability also relates to the muonium formation process and is a temperature-dependent process [78–80]. The increase of the formation probability of the observed muonium state with increasing temperature is reflected in the corresponding decrease of the unobservable fraction of muon spin polarization (missing fraction), the diamagnetic fraction remaining sensibly constant. This missing fraction is associated to muons whose spin polarization is lost during the thermalization process and therefore reflects the presence of another paramagnetic state, either as a precursor or as a final state [78–80]. The diamagnetic fraction is likely associated to muons thermalizing as Mu^+ in oxygen-bond configurations.

In short, these results basically reveal the formation of an atomlike muonium configuration with a hyperfine interaction of 3629(2) MHz at low temperatures, in line with the calculated values for any of the interstitial positions of hydrogen in Lu_2O_3. Together with the muonium state directly observable spectroscopically, there is evidence of the presence of another atomlike state, possibly a precursor configuration. Although the experimental data do not provide a direct identification of the muonium site corresponding to the directly observed state, the fact that this state is formed promptly in the wide temperature range from $T = 7$ K up to $T = 300$ K implies that it corresponds to a very stable configuration, possibly the ground state configuration at the unocc-O site.

IV. CONCLUSIONS

Calculations of the H impurity were carried out in Lu_2O_3 by employing two levels of theory: DFT with the semilocal PBE functional and DFT+U. Whereas within the semilocal approximation the f states of Lu are taken as being core states, with the DFT+U these are correctly treated as localized valence states. DFT+U is an efficient method to address the difficult problem of strongly correlated states, and is also a reliable approach to treat structural relaxations of defective supercells.

Results between the two methods predict similar stable configurations for the impurity, with the neutral H impurity stabilizing at an unoccupied O site, unocc-O, and to a void metal center, void-M_1. The former is lower in energy and therefore the ground-state configuration in the lanthanide oxide. A higher-energy configuration is also predicted, where the hydrogen binds to a neighbor anion O, bond-O configuration. The negative charged systems also indicate a similar energetic stability of the three mentioned configurations. On the other hand, the bond-O configurations are the only possible configurations for the positively charged systems.

From the formation energies, we observed that by taking into account the lowest-energy configurations of the three charge states of H, amphoteric behavior is predicted. DFT+U calculations show that the donor level is positioned above the CBM and the pinning level inside the gap. This indicates that, despite its compensating character, the H electron at the donor configuration is loosely bound to the impurity atom. By comparison, and considering the metastable bond-O configurations (of the three charge states), we observe both pinning level and donor level above the CBM. On the other hand, the plotted isosurfaces of the neutral bond-O configuration indicate a polaron-type character, where the electron from the impurity is trapped at a metal center, and interacting with a portion of the conduction-band states.

The hyperfine interactions have been calculated for the neutral interstitial (unocc-O and void-M_1) configurations of hydrogen leading to isotropic (Fermi-contact) constant equal to 926 and 1061 MHz, respectively. These results are in good agreement with the measurements of muonium spectroscopy which infer a neutral fraction with a strong isotropic hyperfine interaction of similar magnitude.

The good agreement with μSR results regarding the magnitude of the hyperfine constants justifies our choice of the methodology, namely by employing DFT+U. Furthermore, the fact that μSR probes hydrogen states with localized electron densities and high hyperfine constants points out that the pinning level, $E(+/-)$, is indeed inside the band gap as both DFT and DFT+U predict; if $E(+/-)$ crossed inside the conduction band we would obtain a shallow-donor character for hydrogen, in contrast to the DFT+U findings. Therefore, the atomlike and amphoteric character of hydrogen is correctly assessed in the present work, although the exact position of the charge-transition levels still requires experimental verification.

ACKNOWLEDGMENTS

This work was supported with funds from (i) FEDER (Programa Operacional Factores de Competitividade COMPETE) and from FCT-Fundação para a Ciência e Tecnologia under Projects No. PEst-OE/FIS/UI0036/2014 and No. PTDC/FIS/102722/2008, (ii) Ph.D. Grant No. SFRH/BD/87343/2012 from FCT-Fundação para a Ciência e Tecnologia (RBLV), and (iii) Welch Foundation Grant No. D-1321 (TTU group). The authors would also like to thank the computing support from the Department of Physics at the Laboratory for Advanced Computing of the University of Coimbra and from the Department of Chemistry of the University of Bath. Acknowledgements are also to be made to Dr. Marco Molinari of the Department of Chemistry, University of Bath, for fruitful discussions. The technical help of the μSR team at TRIUMF is gratefully acknowledged.

[1] G. Adachi, N. Imanaka, and Z. C. Kang, *Binary Rare Earth Oxides* (Kluwer Academic Publishers, Dordrecht, 2004), Chap. 9.

[2] J. Robertson, High dielectric constant gate oxides for metal oxide Si transistors, Rep. Prog. Phys. **69**, 327 (2006).

[3] P. W. Peacock and J. Robertson, Band offsets and Schottky barrier heights of high dielectric constant oxides, J. Appl. Phys. **92**, 4712 (2002).

[4] L. Tsetseris, D. M. Fleetwood, R. D. Schrimpf, and S. T. Pantelides, in *Defects in Microelectronic Materials and Devices* (CRC Press Taylor & Francis Group, LLC, London, 2009), Chap. 13, pp. 381–398.

[5] J. Robertson, K. Xiong, and K. Tse, in *Defects in Microelectronic Materials and Devices* (Ref. [4]), Chap. 9, pp. 283–303.

[6] K. Xiong, J. Robertson, and S. J. Clark, in *Defects in High-K Gate Dielectric Stacks* (Springer, New York, 2006), pp. 175–187.

[7] C. G. Van de Walle and J. Neugebauer, Hydrogen in semiconductors, Annu. Rev. Mater. Res. **36**, 179 (2006).

[8] R. Alvero, A. Bernal, I. Carrizosa, J. A. Odriozola, and J. M. Trillo, Lanthanide oxides: Lu_2O_3 hydration, J. Less-Common Met. **110**, 425 (1985).

[9] C. G. Van de Walle, Hydrogen as a Cause of Doping in Zinc Oxide, Phys. Rev. Lett. **85**, 1012 (2000).

[10] C. G. Van de Walle, P. J. H. Denteneer, Y. Bar-Yam, and S. T. Pantelides, Theory of hydrogen diffusion and reactions in crystalline silicon, Phys. Rev. B **39**, 10791 (1989).

[11] T. Norby and P. Kofstad, Proton and native-ion conductivities in Y_2O_3 at high temperatures, Solid State Ion. **20**, 169 (1986).

[12] T. Norby and P. Kofstad, Electrical conductivity of Y_2O_3 as a function of oxygen partial pressure in wet and dry atmospheres, J. Am. Ceram. Soc. **69**, 784 (1986).

[13] H. Li and J. Robertson, Behaviour of hydrogen in wide band gap oxides, J. Appl. Phys. **115**, 203708 (2014).

[14] H. Jiang, P. Rinke, and M. Scheffler, Electronic properties of lanthanide oxides from the GW perspective, Phys. Rev. B **86**, 125115 (2012).

[15] L. Ning, Y. Zhang, and Z. Cui, Structural and electronic properties of lutecia from first principles, J. Phys.: Condens. Matter **21**, 455601 (2009).

[16] R. Gilland, S. J. Clark, and J. Robertson, Nature of the electronic band gap in lanthanide oxides, Phys. Rev. B **87**, 125116 (2013).

[17] H. Jiang, R. I. Gomez-Abal, P. Rinke, and M. Scheffler, Localized and Itinerant States in Lanthanide Oxides United by GW@LDA + U, Phys. Rev. Lett. **102**, 126403 (2009).

[18] E. L. Silva, A. G. Marinopoulos, R. C. Vilão, R. B. L. Vieira, H. V. Alberto, J. Piroto Duarte, and J. M. Gil, Hydrogen impurity in yttria: *Ab initio* and μSR perspectives, Phys. Rev. B **85**, 165211 (2012).

[19] A. G. Marinopoulos, Incorporation and migration of hydrogen in yttria-stabilized cubic zirconia: Insights from semilocal and hybrid-functional calculations, Phys. Rev. B **86**, 155144 (2012).

[20] A. Alkauskas, P. Broqvist, and A. Pasquarello, Defect levels through hybrid density functionals: Insights and applications, Phys. Status Solidi B **248**, 775 (2011).

[21] K. Hummler and M. Fähnle, Full-potential linear-muffin-tin-orbital calculations of the magnetic properties of rare-earth–transition-metal intermetallics. I. Description of the formalism and application to the series RC_{O_5} (R = rare-earth atom), Phys. Rev. B **53**, 3272 (1996).

[22] N. Hirosaki, S. Ogata, and C. Kocer, Ab initio calculation of the crystal structure of the lanthanide Ln_2O_3 sesquioxides, J. Alloys Compd. **351**, 31 (2003).

[23] A. Kiejna, G. Kresse, J. Rogal, A. De Sarkar, K. Reuter, and M. Scheffler, Comparison of the full-potential and frozen-core approximation approaches to density-functional calculations of surfaces, Phys. Rev. B **73**, 035404 (2006).

[24] D. A. Andersson, S. I. Simak, N. V. Skorodumova, I. A. Abrikosov, and B. Johansson, Optimization of ionic conductivity in doped ceria, Proc. Natl. Acad. Sci. USA **103**, 3518 (2006).

[25] J. M. Flitcroft, M. Molinari, N. A. Brincat, M. T. Storrb, and S. C. Parker, Hydride ion formation in stoichiometric UO_2, Chem. Commun. **51**, 16209 (2015).

[26] B. Huang, R. Gilland, and J. Robertson, Study of CeO_2 and its native defects by density functional theory with repulsive potential, J. Phys. Chem. C **118**, 24248 (2014).

[27] M. V. Ganduglia-Pirovano, A. Hofmann, and J. Sauer, Oxygen vacancies in transition metal and rare earth oxides: Current state of understanding and remaining challenges, Surf. Sci. Rep. **62**, 219 (2007).

[28] B. Huang, Superiority of DFT+U with non-linear core correction for open-shell binary rare-earth metal oxides: a case study of native point defects in cerium oxides, Philos. Mag. **94**, 3052 (2014).

[29] S. C. Hernandez and E. F. Holby, DFT+U study of chemical impurities in PuO_2, J. Phys. Chem. C **120**, 13095 (2016).

[30] K. Xiong and J. Robertson, Behavior of hydrogen in wide band gap oxides, J. Appl. Phys. **102**, 083710 (2007).

[31] M. D. McCluskey, M. C. Tarun, and S. T. Teklemichael, Hydrogen in oxide semiconductors, J. Mater. Res. **27**, 2190 (2012).

[32] D. M. Hofmann, A. Hofstaetter, F. Leiter, H. Zhou, F. Henecker, B. K. Meyer, S. B. Orlinskii, J. Schmidt, and P. G. Baranov, Hydrogen: A Relevant Shallow Donor in Zinc Oxide, Phys. Rev. Lett. **88**, 045504 (2002).

[33] A. T. Brant, S. Yang, N. C. Giles, and L. E. Halliburton, Hydrogen donors and Ti^{3+} ions in reduced TiO_2 crystals, J. Appl. Phys. **110**, 053714 (2011).

[34] F. Herklotz, E. V. Lavrov, and J. Weber, Infrared absorption of the hydrogen donor in rutile TiO_2, Phys. Rev. B **83**, 235202 (2011).

[35] F. Bekisli, W. Beall Fowler, and M. Stavola, Small polaron characteristics of an OD center in TiO_2 studied by infrared spectroscopy, Phys. Rev. B **86**, 155208 (2012).

[36] S. F. J. Cox, R. L. Lichti, J. S. Lord, E. A. Davis, R. C. Vilão, J. M. Gil, T. D. Veal, and Y. G. Celebi, The first 25 years of semiconductor muonics at ISIS, modelling the electrical activity of hydrogen in inorganic semiconductors and high-κ dielectrics, Phys. Scr. **88**, 068503 (2013).

[37] R. C. Vilão, J. M. Gil, A. Weidinger, H. V. Alberto, J. Piroto Duarte, N. Ayres de Campos, R. L. Lichti, K. H. Chow, and S. F. J. Cox, Information on hydrogen states in II-VI semiconductor compounds from a study of their muonium analogues, Nucl. Instrum. Methods Phys. Res., A **580**, 438 (2007).

[38] R. C. Vilão, A. G. Marinopoulos, R. B. L. Vieira, A. Weidinger, H. V. Alberto, J. Piroto Duarte, J. M. Gil, J. S. Lord, and S. F. J. Cox, Hydrogen impurity in paratellurite α-TeO_2: Muon-spin rotation and *ab initio* studies, Phys. Rev. B **84**, 045201 (2011).

[39] R. B. L. Vieira, R. C. Vilão, P. M. Gordo, A. G. Marinopoulos, H. V. Alberto, J. Piroto Duarte, J. M. Gil, A. Weidinger, and J. S. Lord, Muon-spin-rotation study of yttria-stabilized zirconia (ZrO_2:Y): Evidence for muon and electron separate traps, J. Phys.: Conf. Ser. **551**, 012050 (2014).

[40] R. L. Lichti, K. H. Chow, J. M. Gil, D. L. Stripe, R. C. Vilão, and S. F. J. Cox, Location of the H Level: Experimental limits for muonium, Proceedings of the 23rd International Conference on Defects in Semiconductors [Physica B: Condens. Matter **376-377**, 587 (2006)].

[41] C. G. Van de Walle, Universal alignment of hydrogen levels in semiconductors and insulators, Physica B: Condens. Matter **376–377**, 1 (2006); *Proceedings of the 23rd International Conference on Defects in Semiconductors*, edited by A. Oshiyama, K. Maeda, K. M. Itoh, and H. Katayama-Yoshida (Awaji Island, Japan, 2005).

[42] J. S. Lord, S. F. J. Cox, H. V. Alberto, J. Piroto Duarte, and R. C. Vilão, Double-resonance determination of electron g-factors in muonium shallow-donor states, J. Phys.: Condens. Matter **16**, S4707 (2004).

[43] J. S. Lord, S. P. Cottrell, P. J. C. King, N. Alberto, H. V. Ayres de Campos, J. M. Gil, J. Piroto Duarte, R. C. Vilão, R. L. Lichti, S. K. L. Sjue, B. A. Bailey, A. Weidinger, E. A. Davis, and S. F. J. Cox, Probing the shallow-donor muonium wave function in ZnO and CdS via transferred hyperfine interactions, Physica B: Condens. Matter **308**, 920 (2001).

[44] J. M. Gil, H. V. Alberto, R. C. Vilão, J. Piroto Duarte, N. Ayres de Campos, A. Weidinger, J. Krauser, E. A. Davis, S. P. Cottrell, and S. F. J. Cox, Shallow donor muonium states in II-VI semiconductor compounds, Phys. Rev. B **64**, 075205 (2001).

[45] R. C. Vilão, H. V. Alberto, J. Piroto Duarte, J. M. Gil, A. Weidinger, N. Ayres de Campos, R. L. Lichti, K. H. Chow, and S. F. J. Cox, Muonium spectroscopy in ZnSe: Metastability and conversion, Phys. Rev. B **72**, 235203 (2005).

[46] J. M. Gil, H. V. Alberto, R. C. Vilão, J. Piroto Duarte, N. Ayres de Campos, A. Weidinger, E. A. Davis, and S. F. J. Cox, Muonium states in HgO, J. Phys.: Condens. Matter **13**, L613 (2001).

[47] R. C. Vilão, R. B. L. Vieira, H. V. Alberto, J. M. Gil, A. Weidinger, R. L. Lichti, B. B. Baker, P. W. Mengyan, and J. S. Lord, Muonium donor in rutile TiO_2 and comparison with hydrogen, Phys. Rev. B **92**, 081202 (2015).

[48] F. L. Pratt, WIMDA: A muon data analysis program for the Windows PC, Physica B **289**, 290 (2000).

[49] R. Wyckoff, *Crystal Structures* (Wiley, New York, 1963), Vol. 1.

[50] P. Villars and L. D. Calvert, *Pearson's Handbook of Crystallographic Data for Intermetallic Phases*, 2nd ed. (ASM International, Materials Park, OH, 1991), Vol. IV.

[51] Y.-N. Xu, Z.-Q. Gu, and W. Y. Ching, Electronic, structural, and optical properties of crystalline yttria, Phys. Rev. B **56**, 14993 (1997).

[52] K. Momma and F. Izumi, VESTA: A three-dimensional visualization system for electronic and structural analysis, J. Appl. Crystallogr. **41**, 653 (2008).

[53] J. P. Perdew, K. Burke, and M. Ernzerhof, Generalized Gradient Approximation Made Simple, Phys. Rev. Lett. **77**, 3865 (1996).

[54] S. L. Dudarev, G. A. Botton, S. Y. Savrasov, C. J. Humphreys, and A. P. Sutton, Electron-energy-loss spectra and the structural stability of nickel oxide: An LSDA + U study, Phys. Rev. B **57**, 1505 (1998).

[55] S. Lutfalla, V. Shapovalov, and A. T. Bell, Calibration of the DFT/GGA+U method for determination of reduction energies for transition and rare earth metal oxides of Ti, V, Mo, and Ce, J. Chem. Theory Comput. **7**, 2218 (2011).

[56] G. Kresse and J. Furthmüller, Efficient iterative schemes for *ab initio* total-energy calculations using a plane-wave basis set, Phys. Rev. B **54**, 11169 (1996).

[57] G. Kresse and J. Hafner, *Ab initio* molecular dynamics for liquid metals, Phys. Rev. B **47**, R558 (1993).

[58] G. Kresse and J. Furthmüller, Efficiency of ab-initio total energy calculations for metals and semiconductors using a plane-wave basis set, Comput. Mater. Sci. **6**, 15 (1996).

[59] G. Kresse and D. Joubert, From ultrasoft pseudopotentials to the projector augmented-wave method, Phys. Rev. B **59**, 1758 (1999).

[60] P. E. Blöchl, Projector augmented-wave method, Phys. Rev. B **50**, 17953 (1994).

[61] H. J. Monkhorst and J. D. Pack, Special points for Brillouin-zone integrations, Phys. Rev. B **13**, 5188 (1976).

[62] F. D. Murnaghan, The compressibility of media under extreme pressures, Proc. Natl. Acad. Sci. USA **30**, 244 (1944).

[63] C. G. Van de Walle and J. Neugebauer, Universal alignment of hydrogen levels in semiconductors, insulators and solutions, Nature (London) **423**, 626 (2003).

[64] C. G. Van de Walle and J. Neugebauer, First-principles calculations for defects and impurities: Applications to III-nitrides, J. Appl. Phys. **95**, 3851 (2004).

[65] C. G. Van de Walle, Theory of hydrogen-related levels in semiconductors and oxides, in *Electron Devices Meeting, 2005*, IEDM Technical Digest (IEEE International, New York, 2005), p. 403.

[66] R. M. Nieminen, Issues in first-principles calculations for defects in semiconductors and oxides, Modell. Simul. Mater. Sci. Eng. **17**, 084001 (2009).

[67] K. Szász, T. Hornos, M. Marsman, and A. Gali, Hyperfine coupling of point defects in semiconductors by hybrid density functional calculations: The role of core spin polarization, Phys. Rev. B **88**, 075202 (2013).

[68] VASPwiki. http://cms.mpi.univie.ac.at/wiki/

[69] O. V. Yazyev, I. Tavernelli, L. Helm, and U. Röthlisberger, Core spin-polarization correction in pseudopotential-based electronic structure calculations, Phys. Rev. B **71**, 115110 (2005).

[70] webElements. http://www.webelements.com

[71] M. Perego, G. Seguini, G. Scarel, and M. Fanciulli, X-ray photoelectron spectroscopy study of energy-band alignments of Lu_2O_3 on Ge, Surf. Interface Anal. **38**, 494 (2006).

[72] T. Hattori, T. Yoshida, T. Shiraishi, K. Takahashi, H. Nohira, S. Joumori, K. Nakajima, M. Suzuki, K. Kimura, I. Kashiwagi, C. Ohshima, S. Ohmi, and H. Iwai, Composition, chemical structure, and electronic band structure of rare earth oxide/Si(1 0 0) interfacial transition layer, Microelectron. Eng. **72**, 283 (2004).

[73] P. Erhart, A. Klein, D. Åberg, and B. Sadigh, Efficacy of the DFT+U formalism for modeling hole polarons in perovskite oxides, Phys. Rev. B **90**, 035204 (2014).

[74] P. A. Cox, *Transition Metal Oxides* (Clarendon Press, Oxford, 1992), Chap. 2.

[75] S. F. J. Cox, J. L. Gavartin, J. S. Lord, S. P. Cottrell, J. M. Gil, H. V. Alberto, J. P. Duarte, R. C. Vilão, N. A. de Campos, D. J. Keeble, E. A. Davis, M. Charlton, and D. P. van der Werf, Oxide muonics: II. Modelling the electrical activity of hydrogen

in wide-gap and high-permittivity dielectrics, J. Phys.: Condens. Matter **18**, 1079 (2006).

[76] B. D. Patterson, Muonium states in semiconductors, Rev. Mod. Phys. **60**, 69 (1988).

[77] A. G. Marinopoulos, First principles study of hydrogen configurations at the core of a high angle grain boundary in cubic yttria stabilized zirconia, J. Phys.: Condens. Matter **26**, 025502 (2014).

[78] H. V. Alberto, A. Weidinger, R. C. Vilão, J. Piroto Duarte, J. M. Gil, J. S. Lord, and S. F. J. Cox, Mechanisms of electron polarization of shallow muonium in CdTe and CdS, Phys. Rev. B **81**, 245205 (2010).

[79] H. V. Alberto, R. C. Vilão, J. Piroto Duarte, J. M. Gil, A. Weidinger, J. S. Lord, and S. F. J. Cox, Electron polarization and formation probability of bound muonium in CdS and Si, Phys. Rev. B **86**, 035203 (2012).

[80] R. B. L. Vieira, R. C. Vilão, H. V. Alberto, J. M. Gil, A. Weidinger, B. B. Baker, P. W. Mengyan, and R. L. Lichti, High-field study of muonium states in HfO_2 and ZrO_2, J. Phys.: Conf. Ser. **551**, 012048 (2014).